Spatial Statistics 14 (2015) 563–580

Contents lists available at ScienceDirect

Spatial Statistics

journal homepage: www.elsevier.com/locate/spasta

Spatial point pattern identification of an apparent Ice-Age house structure

Kalanka P. Jayalath [a,*], Richard F. Gunst [a], David J. Meltzer [b]

[a] Department of Statistical Science, Southern Methodist University, P.O. Box 750332, Dallas, TX 75275-0332, USA

[b] Department of Anthropology, Southern Methodist University, P.O. Box 750336, Dallas, TX 75275-0336, USA

ARTICLE INFO

Article history:
Received 19 March 2015
Accepted 7 September 2015
Available online 23 October 2015

Keywords:
Complete spatial randomness
Homogeneous Poisson process
K-function
L-function
Spatial point process

ABSTRACT

Archaeological excavations of a late Ice-Age (Pleistocene) site on the western slope of the Rocky Mountains in Colorado uncovered large rocks that were suspected to be the remains of a house structure. Classical statistical analyses supported this possible conclusion but could not characterize the possible shape of the structure. Analyses using Ripley's *K*-function and an adaptation called the *L*-function confirmed the strong likelihood that the location pattern was not homogeneous across the site. Both nearby regularity and more distant clustering were identified. Circular and elliptical fits to the rock locations were compared using *L*-function simulation envelopes. The simulation envelopes provided strong evidence that the large rocks formed a circular pattern, suggesting that they formed the foundation of a prehistoric house structure.

1. Introduction

Spatial point processes (e.g., Cliff and Ord, 1981; Ripley, 1981; Diggle, 1983; Cressie, 1993; Schabenberger and Gotway, 2004) are widely used to characterize spatial locations of interest. Often the interest is in identifying locations that contain dense clusters of vegetation, insect or animal habitats, or mineral deposits. The focus in this article is on identifying nonrandom patterns of rocks

* Corresponding author.
E-mail addresses: jayalathk@sfasu.edu (K.P. Jayalath), rgunst@smu.edu (R.F. Gunst), dmeltzer@smu.edu (D.J. Meltzer).

http://dx.doi.org/10.1016/j.spasta.2015.09.003
2211-6753/

that could mark the foundation of a prehistoric dwelling at a Late Pleistocene (Ice Age) archaeological site.

Point pattern spatial analysis is of particular value in archaeology, not just in discerning the significance of a spatial pattern and its potential archaeological significance (Miller, 2011) but, as is the case of the Mountaineer archaeological site – the focus of this article – of identifying whether a pattern is cultural in origin or merely a result of natural phenomena. Point pattern statistics in archaeology have been previously applied in a variety of archaeological settings and at multiple spatial scales (Bevan and Conolly, 2006), from the distribution of sites across a region (e.g., Kvamme, 1990; Premo, 2004; Ciminale et al., 2009) to the patterning of objects within individual sites (e.g., MacDonald and Small, 2009; Hill et al., 2011; Miller, 2011; de Smet et al., 2012). Statistical analyses have involved a variety of methods, including the recent application of Ripley's K-function and its transformation to the L-function (e.g., Crema et al., 2010; Miller, 2011), techniques applied to the Mountaineer site rock patterns in this article.

The Mountaineer site is situated atop an isolated, flat mesa located at an elevation of 2625 m above sea level (∼8600 ft) in the Upper Gunnison Basin of Colorado on the western slope of the Rocky Mountains, 50 km from the Continental Divide. The perimeter of the mesa provides a sweeping, virtually unobstructed view of almost 12 km^2 of the surrounding basin. Late Pleistocene hunter–gatherers took notice of this topographic vantage. Archaeological survey of the surface of the mesa top revealed a number of spatially discrete surface artifact clusters, each approximately ∼4–6 m in diameter yielding specimens diagnostic of the Folsom archaeological culture, which is radiocarbon dated to approximately 12,200–12,500 calibrated 14 C years before present (Stiger, 2006; Meltzer, 2009).

Initial excavation of one of those clusters, designated Block A, revealed a concentration of stone artifacts (including diagnostic Folsom projectile points, as well as knives, scrapers and other tools), charcoal, bone and burned mud (clay) daub, all found within and immediately surrounding what appeared to be a roughly circular arrangement of large rocks (>35 cm in maximum dimension) (Stiger, 2006). This discovery was interpreted as the remains of a Folsom-age dwelling, with the large rocks supposed to have formed the foundation and lower walls of the structure, and which presumably anchored wooden poles that served as its upper walls. The inference that the upper walls were made of wood was based on several daub fragments that preserved the rounded form and bark imprint of aspen poles (Stiger, 2006, Fig. 8).

If that interpretation is correct, Mountaineer would be one of the very rare sites from this remote time period to have produced traces of a structure (Irwin-Williams et al., 1973; Frison, 1982; Surovell and Waguespack, 2007; Robinson et al., 2009; Waguespack and Surovell, 2014). The dearth of habitation evidence is due to the fact that the peoples who occupied North America during this time (as well as before and for several millennia afterward) were highly mobile hunter–gatherers who only briefly occupied a place on the landscape, and hence rarely invested the labor required to construct substantial and more lasting dwellings. They were unlike later sedentary groups who occupied the same location for long periods (months, years, and decades) and created a built environment of, for example, adobe or stone (e.g., the well-known prehistoric pueblos of the American southwest).

Yet, however transient Folsom and other early groups were, they assuredly prepared and made use of shelters of some form. The rare archaeological glimpses of their shelters indicate they must have been highly ephemeral structures: little remains of them, save for hints such as post molds (Irwin-Williams et al., 1973; Knudson, 2009), areas of hardened earth interpreted as prepared floors (Frison and Bradley, 1980), bison ribs found driven into the ground below the original surface in a manner to suggest use as tent pegs (Hill, 2008; Frison, 1982, :39-40), or in the spatial distribution and concentration of hearths and artifacts (Surovell and Waguespack, 2007; Hill et al., 2011; Waguespack and Surovell, 2014). In this respect, the possible structure at Mountaineer, with its apparent rock foundation and walls, is especially unusual, if not otherwise unique.

Although the interpretation of the apparent structure at the Mountaineer site as a dwelling is compelling, it is primarily based on a visual examination of the apparently circular arrangement of large rocks, the approximately overlapping area of darkened (presumably anthropogenic) sediment, and relative to them the spatial density and distribution of artifacts, hearths, and other materials (Stiger, 2006). Complicating this interpretation is the fact that the large blocks forming the presumed

Fig. 1. View taken from the south of the Block C area looking north showing it in the initial stages of excavation in 2009. For reference with Fig. 3, this portion of Block C is from grid lines E600 to E608, and from N380 to N388. (Photograph by D.J. Meltzer).

architectural elements are of the same welded volcanic tuff that comprises the near-surface bedrock of the site, and which are strewn across its surface (the Upper Gunnison Basin is one of the coldest regions of North American and is annually subject to harsh freeze-thaw action that fractures the bedrock and shifts the blocks both horizontally and vertically, and hence can potentially arrange their distribution).

The human eye has a strong tendency to see patterns, even where none may exist (Barrow and Bhavsar, 1987; Wunsch, 2006). Visual inspection alone will not suffice to determine a spatial structural pattern amidst a field strewn with naturally broken rocks. The possibility that the distribution of large rocks might be natural rather than anthropogenic must be investigated statistically.

Such an effort is especially imperative in this context, given how rare built architecture is from this time period and the important research questions that will follow if it can be demonstrated that these large rocks were carefully arranged by prehistoric peoples as part of the foundation and wall supports of a dwelling. Questions of interest include: what prompted the investment in labor in construction at this particular site; what might that reveal about the intended (and actual) length of the occupation and the activities that may have taken place here; and why is this site so unusual relative to other sites of this age?

Therefore, following the work at Block A, subsequent excavations at Mountaineer included among the goals an effort to resolve statistically whether the patterning of the large rocks in other of the spatially-discrete surface artifact clusters could be demonstrated to be non-random and cultural and, if so, if the size and shape of that pattern could be discerned in a manner that would provide insight on its purpose. That effort involved intensive excavations in the artifact cluster on a site recorded as Block C, a concentration of Folsom-age artifacts ∼91 m southeast of Block A. Like Block A, the artifacts in Block C were found amidst an abundance of welded tuff blocks.

Fig. 1 is a view of the Block C site in the initial stages of excavation in 2009, after the surface vegetation had been cleared and a portion of the block excavated to a depth of 10 cm. Many large and small rocks are present but there is no discernible pattern that suggests the possible presence of a structure.

In order to make the distribution of the rocks in Block C amenable to spatial statistical analyses, an excavation and mapping protocol was developed to generate detailed point pattern data. All excavations in Block C took place in 5 cm vertical increments within 50 cm^2 quadrants of 1 m^2 units.

Fig. 2. An expanded view of the southeast corner of Block C after subsequent excavations in 2009. The arc of several large, presumed 'house', rocks neighbor other large rocks that could indicate an entryway angling off to the southeast. (Photograph by D.J. Meltzer).

In the course of the excavations, the locations of all rocks greater than or equal to 10 cm but less than 25 cm in maximum dimension were mapped with an EDM Total Station (which provides sub-millimeter accuracy). These rocks, along with any rocks < 10 cm in length, were discarded in order to continue the excavation of that 5 cm excavation level. All rocks ≥ 25 cm were left in place. When the excavation of a particular 5 cm level of a 1 m^2 unit was completed, separate photographs were taken of the floor of each of the four 50 cm^2 quadrants, showing all the rocks in place. The photographs were printed off-site and then returned to the field, after which each rock ≥ 25 cm in length was numbered and its position precisely mapped with the EDM Total Station. Excavations in that unit were then continued down to the next level. The next 5 cm level was excavated, exposing the next level of rocks, and the process of photographing and mapping was repeated. Fig. 2 shows exposed rocks following subsequent excavations in the southeast corner of Block C. The figure shows the emergence of several large neighboring rocks.

Over three seasons of fieldwork in Block C, 120 m^2 were excavated following this protocol, almost two thousand photographs of 50 cm^2 quadrants were taken, and nearly 3900 rocks ≥ 10 cm in length were individually mapped. The emerging overall map of all rocks had considerable spatial noise. It was anticipated, however, that by examining the distribution of the larger rocks, the ones that could have served as foundation or wall stones, might reveal a "signal" amidst the noise, if one existed.

Of the nearly 3900 rocks, 253 rocks were >30 cm in their maximum dimension and deemed large enough, based on experimental evidence, to have served as the foundation or wall supports of a structure (Stiger (2006) used a 35 cm cutoff). These rocks were colloquially designated as "house rocks". Some of their locations are depicted in Fig. 2. Plotting the distribution of all the large rocks

showed they occurred in a roughly circular pattern, which included in the southeast quadrant of the excavation area a particularly well-defined arc of large rocks and an apparent entryway marked by a parallel line of rocks that extended 1.5 m on a bearing of $100^\circ \pm 5^\circ$ toward the rising sun, as indicated in Fig. 2.

Although our focus in this article is on the possible architectural elements of Block C, we note that ∼22,000 stone artifacts, most of which were very small pieces of flaking debris from artifact re-sharpening and manufacture (the total mass of stone artifacts amounts to ∼3 kg), were also recovered from Block C. A small number of formally prepared tools, including both finished projectile points and point preforms were recovered, as well as a variety of processing implements, particularly gravers and scrapers, suggesting that considerable bone and hide working had taken place. The density and distribution of these artifacts generally conformed to an area within and a few meters beyond the roughly circular pattern of large rocks. It is thus of particular importance to demonstrate whether those large rocks are architectural features, which would suggest the presence of artifacts occur both inside and outside the walls of the structure, for that in turn will help enhance our understanding of any spatial patterning to the activities that took place at the site.

The purpose of this article is to investigate the randomness of the spatial locations of 253 large rocks in this excavated site. If a spatial pattern in the large rocks is determined to be nonrandom, a second goal is to characterize the likely shape of the house structure.

2. Investigation of spatial randomness

Complete spatial randomness (CSR) is characterized by spatial processes for which the locations in a region of fixed size and number are independently and uniformly distributed. Homogeneous Poisson processes characterize location counts for regions that exhibit CSR. Extreme deviations from CSR are regions in which the spatial locations occur on a regular grid or regions for which the locations are highly clustered.

2.1. Quadrat-based methods

Lack of spatial randomness is often investigated by counting the number of locations within each of several fixed-area subregions or *quadrats* in a region of interest. Functions of these counts can be meaningfully compared to theoretical values for regions that exhibit CSR. Swindel (1983) proposed a simple calculation for determining the optimal quadrat size (q) for such calculations: $q = 1.6/\hat{\lambda}$. The quantity $\hat{\lambda}$ is an estimate of the density of locations in the region. Diggle (1983, Sec. 3.2.2) recommended estimating the density or *intensity* λ by $\hat{\lambda} = N/|A|$, where N is the number of large rocks and $|A|$ is the area of the region. The region of interest in Block C that encompasses the possible house rocks is 10 m in the easting direction and 9 m in the northing direction. Consequently, $|A| = 90$ m^2 and $\hat{\lambda} = 253/90$, resulting in an optimal quadrat size of 0.75×0.75 m^2. Using this optimal quadrat size, the quadrat counts shown in Fig. 3 were determined.

Quadrat counts range from 0 to 5. A chi-square goodness of fit test ($\chi^2 = 14.01, df = 4, p = 0.007$) rejects the hypothesis that the quadrat counts are a realization of a homogeneous Poisson process; hence, CSR is rejected. Several calculated indices of spatial randomness do not unambiguously indicate violation of CSR. For example, Fisher et al. (1922) relative quadrat variance $I = s^2/\bar{X} = 1.18$, where $\bar{X}$ is the mean and s^2 is the variance of the quadrat counts. This value is fairly close to the theoretical value of 1 for homogeneous Poisson processes. In contrast, Lloyd (1967) mean crowding, $X^* = I + \bar{X} - 1 = 1.80$, indicates that on the average approximately 2 neighboring large rocks share a quadrat with any other large rock. Coupled with the apparent visual circular pattern, the beginning of which is suggested in Fig. 2, this result is consistent with the house rocks being clustered.

The above quadrat analyses fail to make use of spatial similarity or dissimilarity of neighboring quadrats. Greig-Smith (1952) (see also Cressie, 1993; Schabenberger and Gotway, 2004) resize the quadrats so that the number of quadrats is a power of 2. Contiguous quadrats are aggregated in sequentially larger pairs of contiguous blocks, with each block in a pair containing $q = 2^k$ ($k = 1, 2, 3, \ldots$) quadrats. For each block size, analysis of variance mean squares are calculated for the

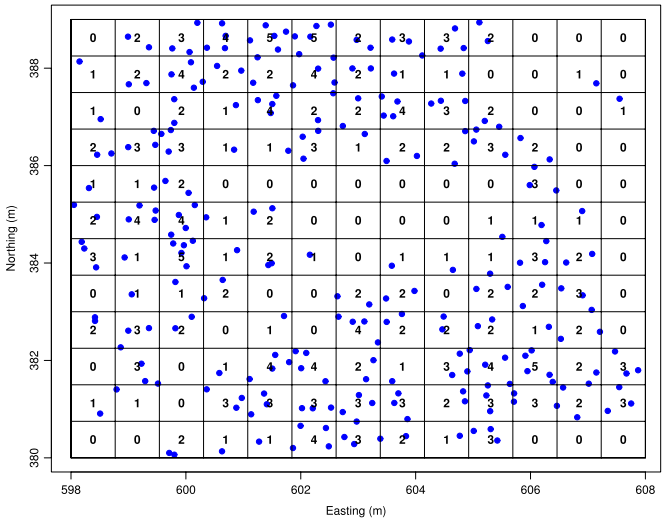

Fig. 3. Quadrat counts of Block C large rocks.

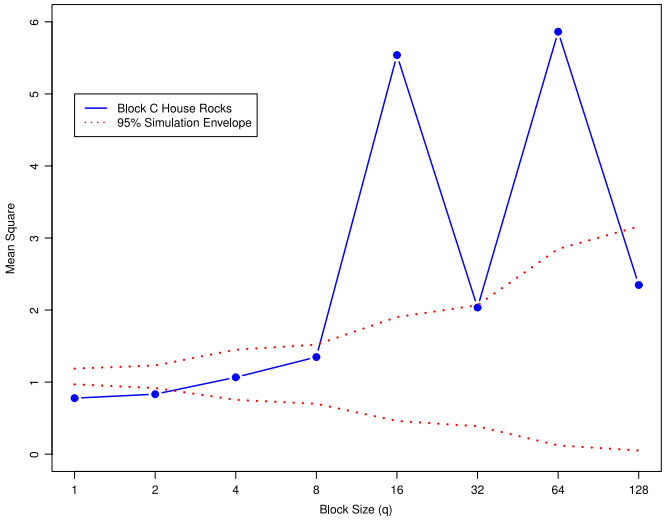

Fig. 4. Mean squares vs. individual block sizes (q) for Block C large rocks.

counts from pairs of neighboring blocks. The Block C quadrats were resized to provide $2^8 = 256$ quadrats of size $10/16 = 0.625$ m by $9/16 = 0.5625$ m and the number of large rocks for each quadrat was determined. Fig. 4 is a plot of the mean squares as a function of the block sizes (q).

One thousand random reassignments of the 253 Block C large rocks were used to calculate the 95% simulation envelopes shown in Fig. 4. If the large rocks in Block C exhibit CSR, the mean squares would be expected to fall between the lower and upper limits of the simulation envelope. The first two block sizes have mean squares that fall below the simulation envelope, indicating that large rocks in close proximity are exhibiting more regularity (or regular dispersion) in location than would be expected under CSR. Mean squares for large rocks in 3 of the 4 largest block sizes are above the simulation envelope, indicating greater clustering than would be expected under CSR. These conclusions support

the chi-square goodness of fit test's rejection of the hypothesis that large rock counts in Block C follow a homogeneous Poisson process, as would be expected under CSR.

2.2. K- and L-function methods

While the Greig-Smith aggregation procedure does make use of neighboring quadrat similarity in counts, none of the previous quadrat procedures directly accommodate the spatial distances among individual rocks. Ripley (1976) and Ripley (1977) introduced a procedure based on second-moment calculations and the spatial intensity λ that can do so. He defined the K-function for a stationary, isotropic point process so that $\lambda K(h)$ is the expected number of additional locations of the process that are within a distance h of any location in a region. There are several variations of the K-function available in the literature, most of which differ depending on whether and how border (i.e., edge) corrections are applied. Ripley estimated $K(h)$ as

$$\hat{K}(h) = \frac{1}{N\hat{\lambda}} \sum_{\substack{i=1 \\ i \neq j}}^{N} \sum_{j=1}^{N} w(s_i, s_j)^{-1} I(\|s_i - s_j\| \leq h). \tag{1}$$

For the Mountaineer large rocks, s_i and s_j are two rock locations, $N = 253$ is the number of large rocks in the region, $I = 1$ if the distance between the rock locations $\|s_i - s_j\| \leq h$ and is 0 otherwise, and $\hat{\lambda} = N/|A| = 2.811$ is the estimated intensity. The edge-correction weight $w(s_i, s_j)$ is not applied since all the large rocks are well within the boundary of Block C; hence, $w(s_i, s_j)$ is set equal to 1. The K-function is calculated for a range of distances h and can be graphed as a function of h.

Besag (1977) recommended graphing a variation of the K-function, the L-function:

$$L(h) = \sqrt{\frac{K(h)}{\pi}} - h. \tag{2}$$

Under an assumption of a homogeneous Poisson process, $K(h) = \pi h^2$ so that the empirical L-function should reasonably approximate a horizontal line centered at zero. A plot of the estimated L-function allows identifying the small-scale regularity, $L(h) < 0$, and large-scale clustering, $L(h) > 0$, in a transformed scale much more clearly than does the K-function. Fig. 5 shows the L-function (Baddeley and Turner, 2005) of the large rocks in Block C. It suggests regularly dispersed rock locations for small and large distances and clustering for intermediate distances between rocks.

A 95% simulation envelope for the L-function (e.g., Baddeley, 2010, Ch. 20) was calculated for the Block C large rocks and is also shown in Fig. 5. The simulation envelope is calculated assuming a homogeneous Poisson process using the estimated intensity function for the Block C large rocks. A comparison of the L-function values for each distance h with the limits of the simulation envelope indicates that large rock locations in Block C show regularity for small distances, less than 0.3 m, and very large distances, greater than 2 m, since the empirical $L(h)$ is below the simulation envelope. Clustering of the Block C large rocks is indicated for distances between approximately 0.4 and 1.4 m, since the empirical $L(h)$ is above the simulation envelope. These conclusions that explicitly use the distances between the large rocks are similar to those using the Greig-Smith quadrat aggregation procedure in Fig. 4.

The primary finding of the foregoing analyses is that the Block C large rocks exhibit both regular dispersion and clustering. This is not a natural feature of randomly scattered rock patterns but is consistent with what would be expected if the large rock locations formed the base of a prehistoric house structure. The broad pattern of large rocks, henceforth referred to as *house rocks*, suggests that perhaps the house structure was circular, primarily due to the low density of large rocks in the center of the region and the high density of rocks at distances equidistant from the center. However, other shapes such as elliptical are also suggested. In the next section, methods for evaluating these possible circular or elliptical shapes are introduced.

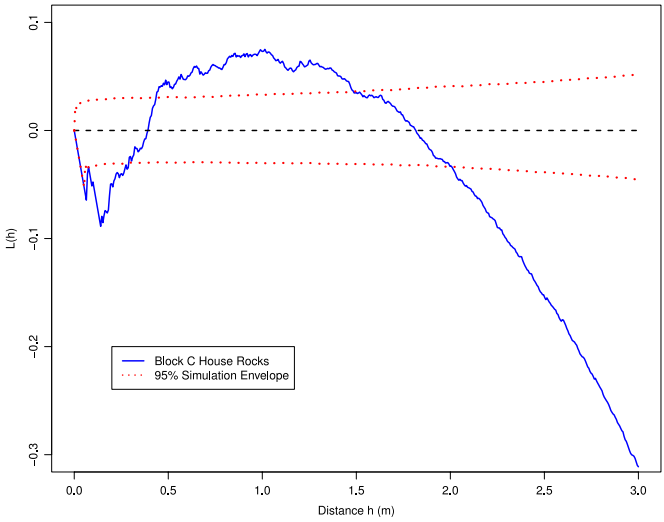

Fig. 5. Empirical L-function curve for Block C large rocks.

3. L-function circular pattern characterization

In this section, L-functions are used to characterize possible circular shapes for the assumed foundation of the Block C house rocks. Characterizations using only large-distance clustering and using both large-distance clustering and small-distance regularity are presented.

3.1. Large-distance clustering

Using geometrical arguments, the theoretical L-function for a perfectly circular structure of radius ρ centered at the origin and lying entirely within a specified region of size $|A|$ can be shown to be

$$L(h) = \sqrt{\frac{|A|}{\pi^2}\cos^{-1}\left(1 - \frac{h^2}{2\rho^2}\right)} - h, \tag{3}$$

where h is the distance between two locations on the circumference of the circle. Fig. 6 contains graphs of the L-function in Eq. (3) for locations lying in a circular pattern centered at the origin within a region of the same size as Fig. 1. Fig. 6(a) displays L-functions for 2000 locations (to produce smooth curves) on circles having radii from 3.2 to 4.4 m. Structures with radii in this range are in keeping with structures known from ethnographic and estimated from hunter–gatherer archaeological contexts, though would be toward the higher end of their range. The largest structure in a sample of 40 such cases compiled by Morgan (2015, Tables 3.3–3.5) had a radius of 4.99 m, with an average radius of ∼2.75 m.

The L-function curves in Fig. 6(a) have similar shapes but are distinguishable. The L-function for a radius of 3.8 m is dashed because it is approximately the radius of the least squares circular fit to the house rocks (see Table 4). Fig. 6(b) consists of L-functions for circles of radius 3.8 m in which the location deviations from the circle are independently normally distributed with mean 0 and standard deviations (σ) increasing from 0.8 to 1.2 m. The L-function for $\sigma = 1$ m is dashed because it is approximately the standard deviation of the least squares circular fit to the house rocks. While the curves are distinctive for small distances, they are very similar over the linear portion for larger distances, especially for the smaller standard deviations; moreover, the curves all intersect at approximately $h = 3.25$ m.

The intersection of all the curves in Fig. 6(b) suggests a method for estimating the radius for circles centered at the origin. Eq. (3) indicates that there is a direct relationship between the L-function and

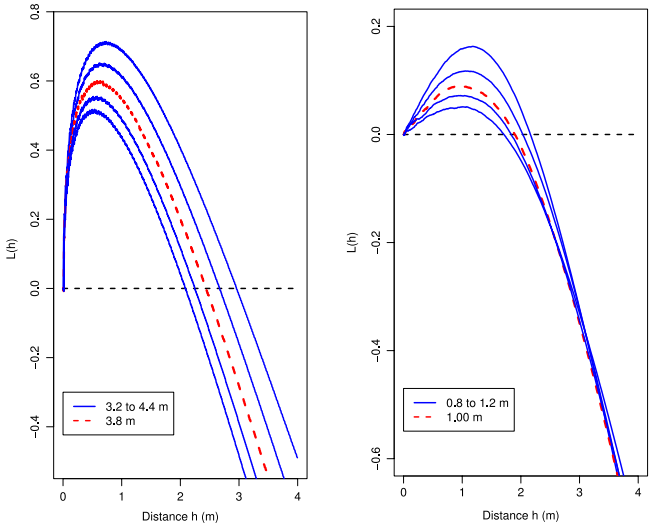

(a) Varying radii. (b) Varying standard deviations.

Fig. 6. *L*-functions for circular rock patterns. (a) No noise ($\sigma = 0$); radii varying from 3.2 m (top) to 4.4 m (bottom) in increments of 0.3 m. (b) Radius 3.8 m; standard deviations varying from $\sigma = 0.8$ m (top) to $\sigma = 1.2$ m (bottom) in increments of 0.1 m.

the radius ρ of the corresponding perfectly circular point processes. The *L*-function can be used to estimate the unknown radius of a perfectly circular point process by solving Eq. (3) for the radius:

$$\rho = \frac{h}{\sqrt{2\left[1 - \cos\left(\frac{\pi^2(L(h)+h)^2}{|A|}\right)\right]}}. \tag{4}$$

Since all the curves in Fig. 6(b) intersect at approximately 3.25 m, solving Eq. (4) at approximately this distance should produce reasonable estimates $\hat{\rho}$ of the radius for all the *L*-functions in the figure.

3.2. Small-distance regularity

L-function values were calculated from Eq. (3) following a thinning of randomly generated circular rock locations. Thinning was accomplished by eliminating simulated locations that were very close together. Nearest-neighbor distances between simulated rock locations were required to be predominantly between 0.15 and 0.45 m, similar to the Block C large rocks. The thinning induced regular dispersion among neighboring rock locations.

Fig. 7 contains *L*-functions calculated for 253 randomly generated locations around a circle of radius 3.8 m with independent additive normally distributed errors with mean 0 and standard deviation 1 m, similar to the least squares estimates for the Block C rock locations (see Sections 4.1 and 5). The solid curve in Fig. 6 is the *L*-function for locations that were not thinned. A 95% simulation envelope for the *L*-function is provided by the dotted curves above and below the solid curve. The primary deviations from the horizontal line for a homogeneous Poisson process are due to clustering at small distances and regularity at very large distances.

The dashed curve in Fig. 7 is the calculated *L*-function for locations that were thinned, inducing regular dispersion. A 95% simulation envelope is provided by the dot–dash curves above and below the dashed curve. The dashed curve illustrates both small-distance regular dispersion, intermediate distance clustering, and large distance regular dispersion similar to the *L*-function in Fig. 5 for the Block C large rocks. A notable feature of the two sets of simulation envelopes is the lack of overlap for

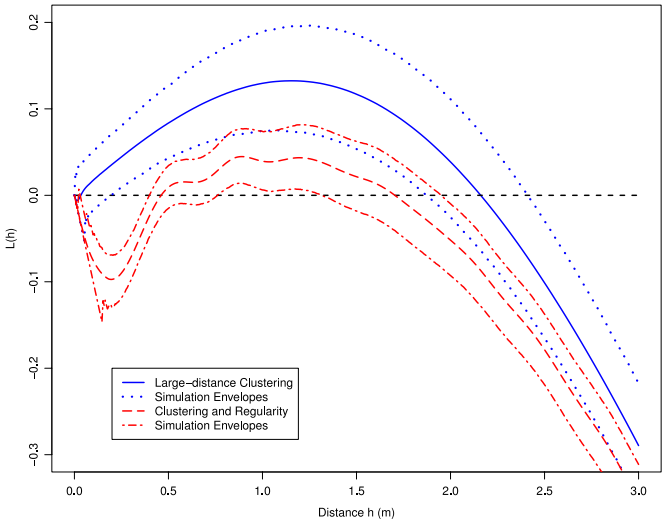

Fig. 7. *L*-functions for circles with large-distance clustering, with and without small-distance regular dispersion.

the smaller distances. This confirms that a sufficiently large initial dip in the *L*-function like in Fig. 5 is a characteristic of regularly dispersed rock locations.

4. Fitting methods and comparisons

Since the pattern of the Block C house rocks is believed to be circular, this section concentrates on fitting circular point processes, with additional investigations of elliptical processes. *L*-function circle characterizations are not easily extended to elliptical shapes; consequently, fitting methods for those processes are presented and compared using simulations.

4.1. Least squares circle fit

Bullock (2006), Pratt (1987), and Taubin (1991), among others, derived methods for fitting circular point processes. One of the most straightforward and easily implemented is Bullock's (2006) least squares circle fit. Let (x_i, y_i) denote a rock location, $u_i = x_i - \bar{x}$, and $v_i = y_i - \bar{y}$. Denote the least squares criterion function for a circle centered at (u_c, v_c) with radius $\rho = \sqrt{\theta}$ as

$$g(u_c, v_c, \theta) = \sum_{i=1}^{n} \{(x_i - u_c)^2 + (y_i - v_c)^2 - \theta\}^2. \tag{5}$$

Let $S_u = \sum u_i$, $S_{uu} = \sum u_i^2$, etc. Differentiating Eq. (5) with respect to u_c and v_c and equating the results to 0 enables the least squares estimates of the center of the circle, $\hat{x}_c = \hat{u}_c + \bar{x}$ and $\hat{y}_c = \hat{v}_c + \bar{y}$, to be obtained by solving

$$\hat{u}_c S_{uu} + \hat{v}_c S_{uv} = (S_{uuu} + S_{uvv})/2 \tag{6}$$

$$\hat{u}_c S_{uu} + \hat{v}_c S_{uv} = (S_{uuu} + S_{uvv})/2 \tag{7}$$

for $\hat{u}_c$ and $\hat{v}_c$. Similarly, differentiating Eq. (5) with respect to θ provides the solution for $\hat{\rho} = \sqrt{\hat{\theta}}$

$$\hat{\theta} = \hat{u}_c^2 + \hat{v}_c^2 + (S_{uu} + S_{vv})/n. \tag{8}$$

Table 1
Means and standard deviations of 1000 radius estimates.

h	3.00			3.25			3.50		
σ	0.75	1.00	1.25	0.75	1.00	1.25	0.75	1.00	1.25
Average	3.96	4.00	4.01	3.91	3.92	3.89	3.87	3.85	3.80
Std.Dev.	0.05	0.08	0.09	0.05	0.07	0.09	0.05	0.07	0.09
h	Across h			3.00	3.25	3.50	Nonlinear		
σ	0.75	1.00	1.25	Across σ			0.75	1.00	1.25
Average	3.91	3.92	3.90	3.99	3.91	3.84	3.93	3.93	3.90
Std.Dev.	0.06	0.09	0.12	0.08	0.07	0.08	0.07	0.09	0.11

4.2. L-function circle fit

When location deviations from a perfectly circular pattern centered at the origin follow a normal probability distribution, Fig. 6(b) illustrates the relatively large differences in L-function curves that can occur for small distances and the nearly coincident linearity for large distances when the standard deviations are sufficiently small. Selecting suitable values of the distance h near the intersection of the curves enables a relatively stable solution for the radius to be obtained for a range of possible standard deviations by using Eq. (4) to obtain an estimate $\hat{\rho}$.

In order to assess the performance of this possible estimation method, simulations were conducted with parameter values similar to those for the least squares fit to the Block C large rocks (see Table 4, Section 5). A total of 1000 simulations were conducted for which 253 rock locations were uniformly generated around a circle centered at the origin with radius 3.8 m. Error variation around the circle followed a zero mean normal probability distribution using three choices for the standard deviation: 0.75, 1.0, and 1.25 m. For each simulation radius estimates $\hat{\rho}$ were calculated from Eq. (4) using h values of 3.0, 3.25, and 3.5 m. The middle value of h was chosen at the approximate distance where all the curves intersect in Fig. 6(b). Summary results are shown in Table 1.

As can be seen from the summary information in the upper portion of Table 1, the empirical L-function provides estimates that are all reasonably close to the true radius $\rho = 3.8$ m. When averaged across the three chosen values of h for each standard deviation in the first 3 columns of the lower portion of the table, or averaged across the three standard deviations for each h in the next 3 columns, the radius estimates remain reasonable. For comparison purposes, the nonlinear *optimize* function in *R* was used to select the best fitting L-function estimate of the radius for each simulated data set using Eq. (3). The algorithm returned the estimated value of ρ that minimized the sum of the squared deviations over a range of h values from 2.75 to 3.75 between the empirical L-function and one calculated using an estimate of ρ. This range of h values was chosen to include most of the linear region for the small standard deviations in Fig. 6(b). As shown in Table 1, the nonlinear estimates were comparable to the other estimates in the table.

4.3. Bayesian circle and ellipse fits

This section details Bayesian methods for fitting possible circular or elliptical rock patterns. The Bayesian model fitting approach is implemented in order to provide point estimates for either the radius of a circle or the major and minor axes lengths of an ellipse. The form of the ellipse that is investigated is:

$$\sqrt{\frac{(x_i - x_c)^2}{a^2} + \frac{(y_i - y_c)^2}{b^2}} - 1 = \epsilon_i \sim N(0, \sigma^2), \tag{9}$$

where (x_c, y_c) is the center of the ellipse and a and b are the lengths of the semi-major and semi-minor axes. This definition of an ellipse includes circular patterns when $a = b = \rho$. Eq. (9) assumes that the locations deviate from an ellipse according to a normal distribution with mean zero and standard deviation σ.

Based on the above relationship, the likelihood function with independent $\epsilon_i \sim N(0, \sigma^2)$, $i = 1, 2, \ldots, n$ can be written as

$$L(\mathbf{x}|\boldsymbol{\Theta}) = \sigma^{-n} \exp\left\{-\sum_{i=1}^{n}\left(\sqrt{\frac{(x_i - x_c)^2}{a^2} + \frac{(y_i - y_c)^2}{b^2}} - 1\right)^2 / 2\sigma^2\right\}. \tag{10}$$

Non-informative priors were selected for each of the unknown parameters. The uniform distribution $U[0, 7]$ is used as the prior distribution of the semi-major and minor axes; the improper prior $1/\sigma^2$ is used as the prior distribution of σ^2; and a bivariate uniform distribution over the sampling window is used as the prior distribution of the center (x_c, y_c). Specifically, the priors are

$$\pi(\sigma^2) \propto \frac{1}{\sigma^2}. \tag{11}$$

$$\pi(a) \propto \text{Uniform}[0, 7]. \tag{12}$$

$$\pi(b) \propto \text{Uniform}[0, 7]. \tag{13}$$

$$\pi(x_c, y_c) \propto \text{Bivariate Uniform}[(598, 608) \times (380, 389)]. \tag{14}$$

In this formulation only the variance parameter (σ^2) has a closed-form posterior (inverse-gamma) distribution:

$$f(\sigma^2|\boldsymbol{\Theta}) \propto \text{Inv–gamma}\left(\text{scale} = \frac{(\mathbf{d} - \mathbf{1})^T(\mathbf{d} - \mathbf{1})}{2}, \text{shape} = \frac{n}{2}\right), \tag{15}$$

where $\mathbf{d}$ is a vector with $d_i = \sqrt{\frac{(x_i - x_c)^2}{a} + \frac{(y_i - y_c)^2}{b}}$, for $i = 1, 2, \ldots, n$. The remaining parameters are updated using a Metropolis–Hastings algorithm.

4.4. Comparisons of circle fits

A simulation study was conducted using 253 generated circular locations with center (0, 0), radius 3.8 m, and $N(0, \sigma^2)$ independent errors, with $\sigma = 0.5$ and 1. In order to examine the effects of non-normal errors, two additional error distributions were examined: the uniform$[-1, 1]$ distribution which is symmetric and relatively short-tailed; and a centralized (mean 0) gamma(2, 2) distribution which is skewed and relatively long tailed. Included in the simulations are the Bayesian, Bullock (2006), L-function, Pratt (1987), and Taubin (1991) circle fits.

The parameter estimates $\hat{\rho}$, and $(\hat{x}_c, \hat{y}_c)$ were directly estimated in the Bullock, Pratt and Taubin methods. The L-function-based estimates of the radius were obtained by using Eq. (4) and the estimates $(\hat{x}_c, \hat{y}_c)$ of the center of the circle were chosen to be the data averages $(\bar{x}, \bar{y})$. For the Bayesian method, the radius and the center were estimated by using posterior medians for each parameter. The simulation study was repeated 1000 times (comparisons of 500 and 1000 simulations yielded very similar results), and sample standard errors for each of the parameter estimates were calculated. The resulting estimates are reported in Table 2.

All five fitting methods provide reasonable mean estimates of the radius parameter. The Bayesian method provides slightly smaller radius estimates for the normal $\sigma = 1$ errors but the mean is still reasonably close to the true radius 3.8 m. As expected, the standard errors for the $\sigma = 1$ errors are larger, approximately twice as large, as those for the $\sigma = 0.5$ errors. All the estimates and standard errors of the center (0, 0) of the circle are reasonable and approximately the same for the various methods. Even though the Bayesian model is explicitly based on assuming normal errors, the simulations using non-normal error structures demonstrate robustness of the Bayesian method, as is true for the other estimation methods across the various error distributions that were examined.

4.5. Comparisons of ellipse fits

Fitzgibbon et al. (1996) proposed an efficient method for fitting ellipses to data. The method minimizes the algebraic distance $\sum_{i=1}^{n} z_i^2$ subject to the constraint $b^2 - 4ac = 1$, where

Table 2
Parameter estimates under different error structures for circular data simulations: estimated average radius $\hat{\rho}$, center $(\hat{x}_c, \hat{y}_c)$, and standard error estimates.

Error	Method	Radius	SE	x_c	SE	y_c	SE
	True	3.80		0.00		0.00	
	Bayesian	3.79	0.03	0.00	0.04	−0.00	0.04
	Bullock	3.82	0.03	0.00	0.04	0.00	0.04
$N(0, 0.5)$	*L*-function	3.86	0.08	0.02	0.03	0.00	0.04
	Pratt	3.87	0.08	0.00	0.04	0.00	0.04
	Taubin	3.82	0.04	0.00	0.04	0.00	0.04
	Bayesian	3.64	0.17	0.00	0.09	0.00	0.09
	Bullock	3.74	0.08	0.00	0.08	0.00	0.08
$N(0, 1)$	*L*-function	3.85	0.11	0.02	0.06	0.00	0.07
	Pratt	3.91	0.13	−0.00	0.09	0.10	0.09
	Taubin	3.74	0.08	0.01	0.08	−0.01	0.09
	Bayesian	3.78	0.04	0.00	0.05	0.01	0.05
	Bullock	3.82	0.04	0.00	0.05	−0.00	0.05
Uniform[−1, 1]	*L*-function	3.87	0.09	0.02	0.03	0.00	0.04
	Pratt	3.90	0.11	0.00	0.05	−0.00	0.05
	Taubin	3.82	0.04	0.00	0.05	−0.00	0.05
	Bayesian	3.70	0.10	−0.00	0.05	0.00	0.05
	Bullock	3.74	0.07	0.00	0.06	0.00	0.06
Gamma(2, 2)	*L*-function	3.78	0.05	0.02	0.04	0.00	0.05
	Pratt	3.83	0.04	0.01	0.07	0.00	0.06
	Taubin	3.74	0.07	0.00	0.07	0.00	0.06

$z_i = ax_i{}^2+bx_iy_i+cy_i{}^2+dx_i+ey_i+f = 0$ is the general form of the conic equation. The method is ellipse-specific, so even non-ellipse data will always return an elliptical fit. The Fitzgibbon et al. method is robust, efficient and easy-to-implement. Similar work can be found in Halir and Flusser (1998). They discussed and extended (Fitzgibbon et al., 1996). Both Halir and Flusser (1998) and Fitzgibbon et al. (1999) provided algorithms that produce numerically stable fits.

Harker et al. (2008) proposed a method to fit specific types of conics to data. Direct and specific fitting of ellipses and hyperbolas is achieved by imposing a quadratic constraint on the conic coefficients. Prasad et al. (2012) introduced a least-squares-based ellipse fitting method that, unlike the previous methods, does not require constrained optimization. The method uses a geometric model of an ellipse and minimizes the geometric distance $|y + \frac{b^2x_0}{a^2y_0}x - \frac{b^2}{y_0}|$ from any point (x, y) on the plane to the closest point (x_0, y_0) on the ellipse $\frac{x^2}{a^2} + \frac{y^2}{b^2} = 1$. The solutions are restricted to ellipses.

Table 3 compares the performance and robustness of the Bayesian, Fitzgibbon et al., Harker et al., and Prasad et al. ellipse-fitting methods. Data are generated from elliptical point patterns with semi-major axis = 3.8 m, semi-minor axis = 3.0 m, and random errors following the same error distributions as with the circle-fitting simulations. The center of the ellipse is located at the origin and the major axis of each elliptical process is rotated 30° from the easting direction. As with the circular processes, 253 locations are used in each simulated elliptical process. The simulation is repeated 1000 times and the average estimates and corresponding standard errors are reported. In the Bayesian method, the average posterior median parameter estimates of both the semi-major and semi-minor axes and of the rotation angle are reported. The rotation angle was determined by a principal components analysis prior to the Bayesian fitting of the other model parameters. The estimates of the center of the ellipse for the various methods were similar to those for the circle fits in Table 2 and are not reported.

Overall the Bayesian, Fitzgibbon et al., and Harker et al. methods performed well in these simulations for all the error distributions. None of these three estimation methods clearly outperformed the others. The Prasad et al. method tended to give the highest estimates for the length of the major axis and the lowest estimates for the length of the minor axis and for the rotation angle. The standard errors for the Prasad et al. method tended to be larger than those for the other methods.

Table 3
Parameter estimates under different error structures for elliptical data simulations: average estimated major (a) and minor (b) axes lengths, rotated angle, and standard error estimates.

Error	Method	a	SE	b	SE	Angle	SE
	True	3.80		3.00		30°	
$N(0, 0.5)$	Bayesian	3.87	0.09	3.14	0.15	29.84°	2.27°
	Fitzgibbon	3.83	0.06	3.11	0.12	29.76°	3.31°
	Harker	3.86	0.09	3.08	0.10	29.76°	4.04°
	Prasad	4.01	0.22	2.90	0.12	19.56°	10.74°
$N(0, 1)$	Bayesian	3.88	0.11	3.38	0.39	27.56°	5.29°
	Fitzgibbon	3.85	0.10	3.25	0.26	25.66°	7.78°
	Harker	3.95	0.20	3.18	0.21	21.86°	12.43°
	Prasad	4.88	1.11	2.73	0.28	9.18°	21.05°
Uniform$[-1, 1]$	Bayesian	3.86	0.08	3.11	0.12	30.10°	1.82°
	Fitzgibbon	3.81	0.05	3.08	0.10	28.08°	3.68°
	Harker	3.84	0.07	3.06	0.08	27.78°	4.41°
	Prasad	4.01	0.21	2.86	0.15	18.27°	11.94°
Gamma$(2, 2)$	Bayesian	3.78	0.06	3.10	0.11	29.88°	2.12°
	Fitzgibbon	3.74	0.09	3.08	0.11	26.07°	6.86°
	Harker	3.79	0.08	3.04	0.09	23.65°	9.18°
	Prasad	4.12	0.34	2.78	0.23	14.12°	16.38°

Table 4
Bayesian, L-function, Bullock, and Taubin circle estimates and Bayesian, Fitzgibbon, and Harker ellipse estimates for large-rock locations in Block C.

Pattern	Method	Radius/major	Minor	Center	Angle
Circle	Bayesian	3.66	–	(602.88, 384.61)	–
	L-function	3.62	–	(602.67, 384.45)	–
	Bullock	3.80	–	(602.84, 384.50)	–
	Taubin	3.80	–	(602.87, 384.51)	–
Ellipse	Bayesian	3.91	3.65	(602.82, 384.48)	128°
	Fitzgibbon	4.03	3.51	(602.82, 384.52)	142°
	Harker	4.22	3.45	(602.82, 384.52)	167°

5. Block C house rocks structural shape

5.1. Circle and ellipse fits to the Block C house rocks

Table 4 displays the parameters estimated for the circular and elliptical fits to the Block C house rocks. The Bullock and Taubin et al. circular fits are virtually identical, with estimated radii 3.80 m. The Bayesian and L-function estimates of the radius are slightly smaller, approximately 3.6 m.

The Bayesian, Fitzgibbon et al., and Harker et al. ellipse parameter estimates are also shown in Table 4. The Prasad et al. estimates were markedly different from the true parameter values in the simulations reported in the last section and are not included. There are differences in the parameter estimates for the major and minor axis lengths and the angle of rotation but all the estimates are reasonably similar. The next two sections summarize assessments of the various circle and ellipse fits.

5.2. Reasonableness of model assumptions

Bullock's (2006) least squares circle fit estimated the radius and center of the Block C large-rock locations to be 3.8 m and grid coordinates East 602.84, North 384.50, respectively. The fitted circle is shown in Fig. 8 as the solid curve. The fitted L-function circle is shown as the dashed curve for comparison. Visually the curves are very similar and appear to capture the center of the curved rock formation well. The other two circular fits overlap these two fits.

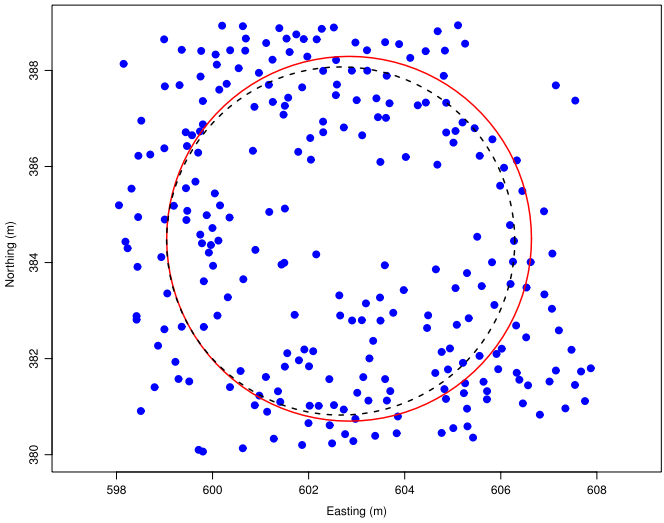

Fig. 8. Spatial distribution of Block C large rocks with least squares (solid) and *L*-function (dashed) circle fits superimposed.

The distances of the Block C large-rock locations from the fitted least squares circle appear to be normally distributed in the histogram in Fig. 9(a). An important interpretive feature of the histogram is the tapering of the number of rocks in both radial directions from the fitted circle, suggesting the presence of areas cleared of large rocks on both sides of what was likely the collapsed wall of the structure. The tapering in the negative direction supports the concept of cleared living surface in the center of the house, as is to be expected within a dwelling.

The standard deviation of the fitted circle was estimated using the minimum distance from the center of each rock to the least squares circle. The estimated standard deviation for Block C large-rock deviations from the fitted circle is 1.04 m. Standard deviation estimates from the other fitted circles and ellipses were similar.

The quantile plot in Fig. 9(b) also supports the assumption of normally distributed radial large-rock distances from the fitted circle. Superimposed on the quantile plot is a 95% simulation envelope for the quantiles. The envelope values were simulated from a normal probability distribution with the same mean and standard deviation as those estimated using the least square circle fit. The empirical quantile plot values are on or within the envelope values.

5.3. Simulation envelope comparisons of circle and elliptical fits

One assessment of whether any of the circle or ellipse fits are reasonable can be made by randomly simulating rock locations from the various fits using the estimated parameters and then comparing the actual Block C empirical *L*-function with 95% simulation envelope limits for each fit. Fig. 10 shows the envelopes from the various model fits in Table 4 using normal errors having standard deviations estimated from the fits. As with the simulation envelope for the quantile plot in Fig. 9, if the Block C empirical *L*-function is within the simulation envelope for a fit, the corresponding fit exhibits fidelity to the characterized rock pattern.

The dashed curves in the figures are the 95% simulation envelope limits. The solid curves between the limits are the means of the envelopes. The circle fits all have upper simulation limits that are approximately the same as the Block C empirical *L*-function values for small distances, approximately 1 m or less. The empirical *L*-function is well within the simulation limits for larger distances and approximately equal to the mean envelope values for the Bayesian and *L*-function fits. In contrast, all of the ellipse fits have upper simulation envelope values that are well below the empirical *L*-function values.

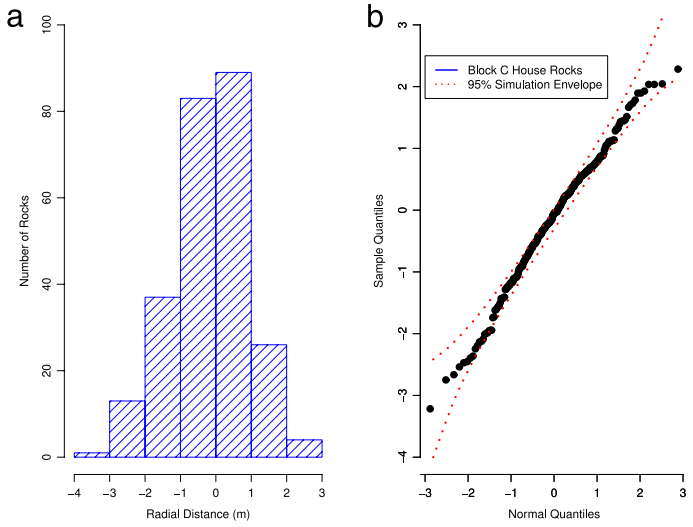

Fig. 9. Summary of Euclidian distances of Block C large rocks: (a) Histogram of distances, (b) Normal quantile plot of distances.

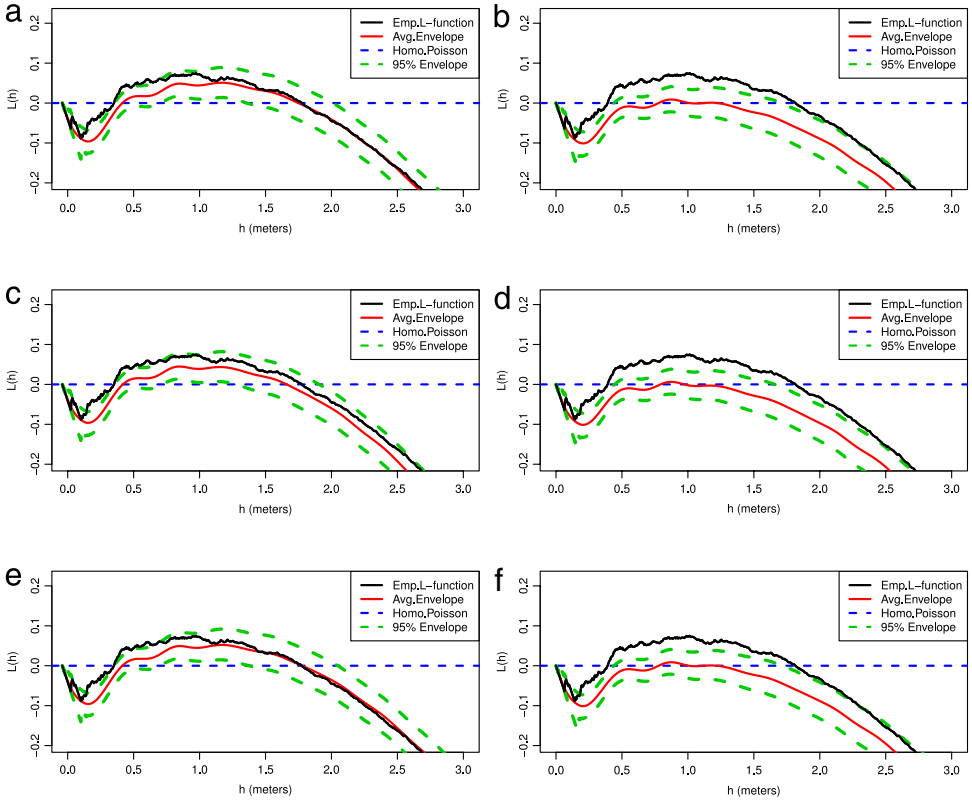

Fig. 10. Simulation envelopes for fits to Block C large rocks: (a) Bayesian circle, (b) Bayesian ellipse, (c) Bullock and Taubin circle, (d) Harker ellipse, (e) *L*-function circle, (f) Fitzgibbon ellipse.

6. Discussion

Calculation of the empirical *L*-function is a powerful method for discriminating between alternative possible rock patterns. Fig. 5 demonstrates that the *L*-function provides much more information than simply a conclusion that the Block C house rock locations are not spatially homogeneous. The deviations of the *L*-function from the simulation envelope identify small distances at which the rock locations are so close to one another they characterize a regular pattern and larger distances where they appear to be clustered relative to one another around the circular pattern. For the largest distances, those approaching the radius of the fitted circle, they are once again characterized as exhibiting a regular pattern. Moreover, Fig. 7 demonstrates that the regularity and clustering in the *L*-function for the Block C house rocks can be reproduced through random simulation of the characterized patterns.

The 253 large rocks within Block C at the Mountaineer site are nonrandom in their distribution, suggesting they were moved into position by human activity which, based on the broadly conforming density and distribution of artifacts, would suggest the presence of a structure. Analysis of circular and elliptical patterns of the Block C house rocks provides strong evidence that the pattern of the house structure was circular, roughly 3.8 m in diameter, with its central area cleared of large rocks, which are instead regularly dispersed at close radii several meters out from the center and likely mark the collapsed walls of the dwelling.

The demonstrated presence of such a structure in Block C cannot confirm the inference that a like structure was present in Block A. Nonetheless, the very similar patterning of artifacts and large rocks in both blocks, along with the telling evidence of structural elements in Block A (e.g. the aspen pole-impressed daub fragments), would suggest there are multiple houses at the Mountaineer site. As noted at the outset, that makes the Mountaineer site an extremely rare – if not unique – example from this time period of substantial, non-ephemeral and (we presume), labor-intensive built architecture, implying a longer residence here than is customary among these highly mobile groups. Why that took place at this location and seemingly no other place on the Late Pleistocene landscape, and what it represents in terms of the activities (indoors and out) and adaptations of this group of Folsom hunter–gatherers, can now be better addressed with the spatial statistical demonstration these were not merely natural rock alignments but purposefully constructed houses.

Acknowledgments

All the calculations and simulations reported in this article were based on code adapted from the *R Foundation for Statistical Computing* (R Core Team, 2013). Excavations at the Mountaineer site were undertaken in collaboration with Mark Stiger (Western State Colorado University). The work at Block C was funded by the Quest Archaeological Research Program of the Department of Anthropology, Southern Methodist University, under the direction of D. Meltzer. We would like to thank the graduate student crews who, over several seasons of fieldwork at the site, took on with good humor the somewhat tedious task of mapping many thousands of rocks in order to provide the data necessary for this study.

References

Baddeley, A., 2010. Analyzing spatial point patterns in R. In: Case Studies in Spatial Point Pattern Modeling. CSIRO and University of Western Australia, Western Australia, pp. 23–74.

Baddeley, A., Turner, R., 2005. Spatstat: an R package for analyzing spatial point patterns. J. Stat. Softw. (ISSN: 1548-7660) 12, 1–42.

Barrow, J.D., Bhavsar, S.P., 1987. Filaments-what the astronomer's eye tells the astronomer's brain. Q. J. R. Astron. Soc. 28, 109.

Besag, J.E., 1977. Comment on modeling spatial point processes by B.D. Ripley. J. R. Stat. Soc. Ser. B 39, 193–195.

Bevan, A., Conolly, J., 2006. Multiscalar approaches to settlement pattern analysis. In: Confronting Scale in Archaeology. Springer, pp. 217–234.

Bullock, R., 2006. Least squares circle fit. URL: www.dtcenter.org/met/users/docs/write_ups/circle_fit.pdf.

Ciminale, M., Gallo, D., Lasaponara, R., Masini, N., 2009. A multiscale approach for reconstructing archaeological landscapes: Applications in Northern Apulia (Italy). Archaeol. Prospect. 16, 143–153.

Cliff, A.D., Ord, J.K., 1981. Spatial Processes: Models and Applications. Pion, London.

Crema, E.R., Bevan, A., Lake, M.W., 2010. A probabilistic framework for assessing spatio-temporal point patterns in the archaeological record. J. Archaeol. Sci. 37, 1118–1130.
Cressie, N.A.C., 1993. Statistics for Spatial Data. Wiley, New York.
de Smet, T.S., Everett, M.E., Pierce, C.J., Pertermann, D.L., Dickson, D.B., 2012. Electromagnetic induction in subsurface metal targets: Cluster analysis using local point-pattern spatial statistics. Geophysics 77, WB161–WB169.
Diggle, P., 1983. Statistical Analysis of Spatial Point Patterns. Academic Press, Western Australia.
Fisher, R.A., Thornton, H.G., Mackenzie, W.A., 1922. The accuracy of the plating method of estimating the density of bacterial populations. Ann. Appl. Biol. 9, 325–359.
Fitzgibbon, A.W., Pilu, M., Fisher, R.B., 1996. Direct least squares fitting of ellipses. In: IEEE Proceedings of the 13th International Conference on Pattern Recognition, Vol. 1, pp. 253–257.
Fitzgibbon, A.W., Pilu, M., Fisher, R.B., 1999. Direct least square fitting of ellipses. IEEE Trans. Pattern Anal. Mach. Intell. 21, 477.
Frison, G.C., 1982. Folsom components. In: Frison, G.C., Stanford, D. (Eds.), Agate Basin Site: A Record of the Paleoindian Occupation of the Northwestern High Plains. Academic Press, New York, pp. 37–76.
Frison, G.C., Bradley, B., 1980. Folsom Tools and Technology of the Hanson Site, Wyoming. University of New Mexico Press, Albuquerque.
Greig-Smith, P., 1952. The use of random and contiguous quadrats in the study of the structure of plant communities. Ann. Bot. 16, 293–316.
Halir, R., Flusser, J., 1998. Numerically stable direct least squares fitting of ellipses. In: The Sixth International Conference in Central Europe on Computer Graphics and Visualization, pp. 59–108.
Harker, M., O'Leary, P., Zsombor-Murray, P., 2008. Direct type-specific conic fitting and eigenvalue bias correction. Image Vis. Comput. 26, 372–381.
Hill, M.G., 2008. Paleoindian Subsistence Dynamics on the Northwestern Great Plains: Zooarchaeology of the Agate Basin and Clary Ranch Sites, Oxford: British Archaeological Reports International Series 1756.
Hill, M.G., Rapson, D.J., Loebel, T.J., May, D.W., 2011. Site structure and activity organization at a Late Paleoindian base camp in Western Nebraska. Am. Antiquity 752–772.
Irwin-Williams, C., Irwin, H., Agogino, G., Haynes, C.V., 1973. Hell gap: Paleo-Indian occupation on the high plains. Plains Anthropol. 40–53.
Knudson, R., 2009. The early expeditions: University of Wyoming, Harvard University, and the Peabody Museum. In: Larson, M.L., Kornfeld, M., Frison, G.C. (Eds.), Hell Gap: A Stratified Paleoindian Campsite at the Edge of the Rockies. University of New Mexico Press, Albuquerque, pp. 14–35.
Kvamme, K.L., 1990. Spatial autocorrelation and the Classic Maya collapse revisited: Refined techniques and new conclusions. J. Archaeol. Sci. 17, 197–207.
Lloyd, M., 1967. Mean crowding. J. Anim. Ecol. 36, 1–30.
MacDonald, J.A., Small, M.J., 2009. Statistical analysis of metallic anomaly patterns at former air force bombing ranges. Stoch. Environ. Res. Risk Assess. 23, 203–214.
Meltzer, D.J., 2009. First Peoples in a New World: Colonizing Ice Age America. Univ. of California Press, Berkeley.
Miller, M.R., 2011. Estimating site structure and site occupation span using point pattern spatial analysis: Interpretations of surface artifact distributions at the El Arenal site, El Paso County, Texas. Bull. Tex. Archeol. Soc. 82, 193–222.
Morgan, B.M., 2015. Folsom settlement organization in the southern Rocky Mountains: an analysis of dwelling space at the Mountaineer site (Ph.d. dissertation), Department of Anthropology, Southern Methodist University, Dallas, TX.
Prasad, D.K., Leung, M.K.H., Quek, C., 2012. ElliFit: An unconstrained, non-iterative, least squares based geometric ellipse fitting method. Pattern Recognit. 49, 1449–1465.
Pratt, V., 1987. Direct least-squares fitting of algebraic surfaces. Comput. Graph. 21, 145–152.
Premo, L.S., 2004. Local spatial autocorrelation statistics quantify multi-scale patterns in distributional data: An example from the Maya Lowlands. J. Archaeol. Sci. 31, 855–866.
R Core Team, 2013. R: A Language and Environment for Statistical Computing. R Foundation for Statistical Computing, Vienna, Austria.
Ripley, B.D., 1976. The second-order analysis of stationary point processes. J. Appl. Probab. 13, 255–266.
Ripley, B.D., 1977. Modeling spatial patterns. J. R. Stat. Soc. Ser. B 39, 172–192.
Ripley, B.D., 1981. Spatial Statistics. Wiley, New York.
Robinson, B.S., Ort, J.C., Eldridge, W.A., Burke, A.L., Pelletier, B.G., 2009. Paleoindian aggregation and social context at Bull Brook. Am. Antiquity 423–447.
Schabenberger, O., Gotway, C.A., 2004. Statistical Methods for Spatial Data Analysis. Chapman & Hall/CRC, Boca Raton, FL.
Stiger, M., 2006. A Folsom structure in the Colorado Mountains. Am. Antiquity 71, 321–351.
Surovell, T.A., Waguespack, N.M., 2007. Folsom hearth-centered use of space at Barger Gulch, Locality B. In: Brunswig, R.S., Pitblado, B. (Eds.), Emerging Frontiers in Colorado Paleoindian Archaeology. University of Colorado Press, Boulder, pp. 219–259.
Swindel, B.F., 1983. Choice of size and number of quadrats to estimate density from frequency in Poisson and binomially dispersed populations. Biometrics 39, 455–464.
Taubin, G., 1991. Estimation of planar curves, surfaces, and non-planar space curves defined by implicit equations with applications to edge and range image segmentation. IEEE Trans. Pattern Anal. Mach. Intell. 13, 1115–1138.
Waguespack, N.M., Surovell, T.A., 2014. A simple method for identifying households using lithic assemblages: A case study from a Folsom campsite in Middle Park, Colorado. In: MacDonald, D.H., Andrefsky Jr., W., Yu, P.-L. (Eds.), Lithics in the West: Using Lithic Analysis to Solve Archaeological Problems in Western North America. University of Montana Press, Missoula, pp. 35–49.
Wunsch, C., 2006. Abrupt climate change: An alternative view. Quat. Res. 65, 191–203.